Between waves and patterns: Spin wave freezing in films with Dzyaloshinskii-Moriya interaction

Jan Kisielewski [1,*] Paweł Gruszecki [2] Maciej Krawczyk [2] Vitalii Zablotskii [3] and Andrzej Maziewski [1]

[1]*Faculty of Physics, University of Białystok, Białystok, Poland*
[2]*Faculty of Physics, Adam Mickiewicz University, Poznań, Poland*
[3]*Institute of Physics, Czech Academy of Sciences, Prague, Czech Republic*

The relationship between waves and static pattern formation is an intriguing effect and remains unexplained in many areas of physics, including magnetism. We study the spin-wave-mediated spin reorientation transition (SRT) in magnetic films with uniaxial magnetic anisotropy and Dzyaloshinskii-Moriya interaction (DMI). In particular, we show that propagating spin waves can freeze in the SRT, causing periodic magnetic domains to arise, which is reminiscent of the wave amplitude distribution. This process can take place under the influence of a change in the magnetic field, but also of other parameters. Interestingly, at the SRT, DMI nonreciprocity leads to the emergence of flowing magnetization patterns, which suggests a spontaneous breaking of translational symmetry, and the formation of magnonic space-time crystals. The described phenomena are general and should take place in a large family of magnetic materials. Therefore, the results should be of great importance for the further development of spintronics and magnonics.

I. INTRODUCTION

Pattern formation mediated by collective harmonic oscillations is an intriguing phenomenon that combines linear equilibrium dynamics and spontaneously broken translational symmetry that occurs in nonlinear phase transitions. The effect is quite common in nature and has been observed in hydrodynamic systems as thermal convection or parametric-wave instabilities, nonlinear optics, chemical reactions, and biological systems [1–4]. Research on the subject has recently extended to nonreciprocal systems, where the role of time-reversal symmetry breaking in the self-organization process has been studied, and interesting collective phenomena, such as time crystals, synchronization, or flowing patterns, have been observed [5,6].

Phase transitions in ferromagnetic materials include those between a paramagnetic and a magnetically ordered state, and the domain nucleation process, which leads to the stabilization of irregular or regular domain structures [7]. The domain structure is usually determined by the interplay between the magnetostatic interaction, magnetic anisotropy, the exchange interaction, and the magnetic and thermal history. Due to strong spin-orbit interactions at the interface between ultrathin ferromagnets and nonmagnetic metals, Dzyaloshinskii-Moriya anisotropic exchange interaction (DMI) can result in a chiral magnetization distribution [8].

Spin waves (SWs), propagating coherent disturbances of magnetization, are considered as prospective information carriers [9–11]. Most research on the propagation of SWs is devoted to their propagation in uniform or nanostructured media, such as through the use of different hole arrangements [12–14]. However, in recent years inhomogeneous magnetization textures have been recognized as promising media with unique properties [15–19]. For SWs propagating perpendicularly to the static magnetization direction [i.e., in the Damon-Eshbach (DE) geometry] in thin films with uniaxial magnetic anisotropy, the SW dispersion relation can be nonmonotonic, with a minimum at the wave number $k \neq 0$ [15]. When decreasing the bias magnetic field, this minimum can reach a near-zero frequency in a process known as mode softening, followed by magnetization instability, which initiates a spin reorientation transition (SRT) with spatial symmetry breaking. In mode softening, the impact of the spatial SW amplitude distribution on the stable magnetization domain pattern of various types has been confirmed in micromagnetic simulations for a ferromagnet bar, a ferromagnetic stripe, an elliptical nanodot, and recently ultrathin magnetic film with DMI [20–23]. Also, the magnetization instability at the edge of the film resulting in skyrmion nucleation is predicted to be initiated by the edge-localized SWs [24]. Moreover, stripe domain patterns in fields just below the SRT are systems in which Higgs and Goldstone modes, both related to translational symmetry breaking, have been observed recently [25]. However, the interplay between magnetization dynamics and a static magnetization configuration, in particular the role of SWs in the formation of regular magnetization patterns [21,26], and the influence of magnetic anisotropy and film thickness, remain largely unexplored. Furthermore, the effect of DMI-induced nonreciprocity [27–31] on the mode softening and on the SRT, i.e., the influence of time-reversal symmetry breaking on SW-mediated pattern formation, has not been studied yet.

Here, we address the above-mentioned questions and problems, showing the close relationship between the spatial

*jankis@uwb.edu.pl

distribution of the SW amplitude at the SRT and the magnetic domain structure stabilizing after the transition. Using micromagnetic simulations, we numerically characterize the SW-freezing process that leads to the translational symmetry breaking at the SRT, and we determine analytical conditions of this domain nucleation process. The possibility of observing flowing stripe domain patterns during the SRT in ferromagnetic thin films with the nonreciprocal dispersion relation is also demonstrated. To generalize our conclusions, we present the behavior of SWs while approaching SRTs induced by the magnetic field, magnetic anisotropy, DMI constant, and film thickness. We show that homogeneous thin and ultrathin films with uniaxial magnetic anisotropy and DMI are an excellent platform for studying phase transitions and pattern formation (magnetization). Therefore, our results are not only promising from an application point of view in magnonics and spintronics, but they also reveal the relationship between waves and static patterns exemplified by SWs and magnetization texture occurring at ambient temperature and available for testing with state-of-the-art experimental techniques.

II. SPIN WAVE SOFTENING

Ferromagnetic films with uniaxial magnetic anisotropy are usually characterized by the following: (i) their thickness d, (ii) magnetic anisotropy K_u [that can by expressed as the quality factor $Q = 2K_u/(\mu_0 M_s^2)$, where M_s is the saturation magnetization], (iii) exchange constant A_{ex} [that can be used as the exchange length, $l_{ex} = \sqrt{2A_{ex}/(\mu_0 M_s^2)}$], and (iv) DMI coefficient D [that can be used, similarly, as the DMI length, $l_{DM} = 2D/(\mu_0 M_s^2)$]. The magnitudes of d, Q, D, and the external magnetic field H determine stable magnetization configurations; thus they are of particular interest while approaching an SRT, at critical values denoted by an asterisk, H^*, Q^*, D^* or d^*. For instance, a field-induced SRT (H-SRT) occurs while the in-plane magnetic field H, applied to an initially in-plane saturated sample, decreases below its critical value H^*. Both H-SRT and Q-SRT (Q-induced SRT) have already been studied in ultrathin films by micromagnetic simulations and in the sinusoidal-like stripe domain approach [32,33]. Magnetic ultrathin films with $Q < 1$ are typically in-plane magnetized at remanence; however, they can undergo a d-SRT when their thickness increases above d^*. Finally, a D-SRT can occur when the DMI constant is increased above its critical value D^* [34].

The dispersion relation in the DE geometry in thin films with a homogeneous in-plane magnetization with contributions from the magnetostatic interaction, the uniaxial magnetic anisotropy, the exchange interaction, and the DMI [29,30,35,36] can be expressed in reduced parameters (see Table I in Appendix F) as follows:

$$f(\kappa) = f_0\left[\sqrt{\left(h + \frac{\kappa^2}{d_{ex}^2} + \xi(|\kappa|)\right)\left(h + \frac{\kappa^2}{d_{ex}^2} - \xi(|\kappa|) - Q + 1\right)} + \frac{D_{ex}}{d_{ex}}\kappa\right], \tag{1}$$

where $\xi(\kappa) = 1 - [1 - \exp(-\kappa)]/\kappa$, $\kappa = kd$ is a dimensionless wave number (more precisely, the units of κ are radians, but this fact does not affect any following derivations or numbers). Quantities $d_{ex} = d/l_{ex}$ and $D_{ex} = l_{DM}/l_{ex}$ are the reduced thickness and the reduced DMI length, respectively, both related to the exchange length, and $h = H/M_s$ is the dimensionless in-plane applied magnetic field. The frequency f is reduced by a factor $f_0 = \gamma\mu_0 M_s/(2\pi)$. Thus, we will henceforth use the reduced parameters h^*, d_{ex}^*, and D_{ex}^* (instead of H^*, d^*, and D^*, respectively) also for the description of the respective SRTs.

Let us consider the following general conditions:

$$\frac{df(\kappa)}{d\kappa} = 0, \tag{2a}$$

$$f(\kappa) = 0, \tag{2b}$$

describing the vanishing of the SW group and phase velocities for nonzero wave numbers. Simultaneous vanishing takes place at a critical wave number κ^*. We will show that at this point the magnetization structure becomes unstable, which assists an SRT and leads to the formation of stripe domain patterns. Thus, the parameters that satisfy the conditions Eqs. (2a) and (2b) will henceforth be called critical and denoted by an asterisk. Searching for relationships between these parameters and the material constants when approaching the SRT is one of the main subjects of this study. In

the following sections, we will analyze the conditions of the instability, the factors influencing the SRT process, and the relation between the SW mode and the relaxed magnetization stripe domains formed after crossing the SRT, especially the critical SW wavelength and the critical period of the nucleated domain structure, Λ^* and p^*, respectively. Expressed in reduced units, they are both $\Lambda_{ex}^* = \Lambda^*/l_{ex}$ and $p_{ex}^* = p^*/l_{ex}$.

Considering Eq. (1) in an ultrathin film [$\kappa \ll 1$, so $\xi(\kappa) \approx |\kappa|/2$] without DMI, the solution of Eqs. (2a) and (2b) leads to the following formula for the critical field:

$$h^* = Q - 1 + \frac{d_{ex}^2}{16}. \tag{3a}$$

This applies to the case of H-SRT, i.e., when h is a free parameter, while the others are arbitrary. If we fix $h = 0$, then

$$Q^* = 1 - \frac{d_{ex}^2}{16}, \tag{3b}$$

which corresponds to a Q-SRT at remanence. In both cases, the critical SW wavelength is

$$\Lambda_{ex}^* = \frac{2\pi d_{ex}}{\kappa^*} = \frac{8\pi}{d_{ex}}, \tag{3c}$$

and this formula is valid for both H-SRT and Q-SRT mentioned above. Note that these relationships obtained from an SW analysis and determining the critical values Q^* and Λ_{ex}^* [Eqs. (3b) and (3c)] are the same as Q^* and p_{ex}^* reported in
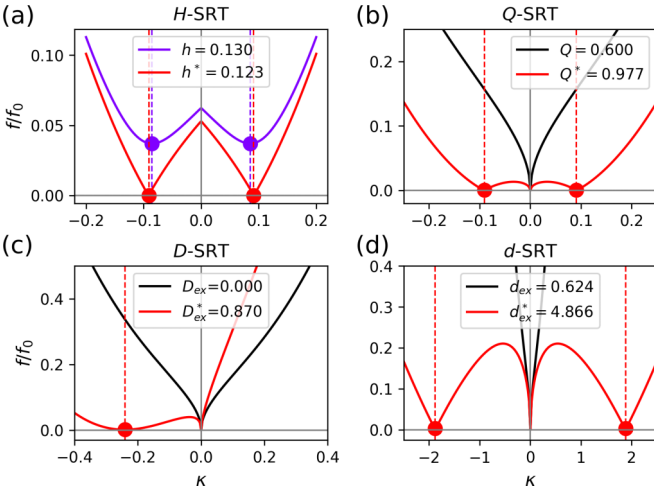
FIG. 1. Analytical dispersion relations constructed with Eq. (1) illustrating conditions required for SRT occurrence. (a) H-SRT for $Q = 1.1$, $D_{ex} = 0$, and $d_{ex} = 0.624$; (b) Q-SRT for $h = 0$, $D_{ex} = 0$, and $d_{ex} = 0.624$; (c) D-SRT for $h = 0$, $Q = 0.6$, and $d_{ex} = 0.624$; (d) d-SRT for $h = 0$, $Q = 0.6$, and $D_{ex} = 0$. Black lines in (b)–(d) pertain to the same set of parameters ($h = 0$, $Q = 0.6$, $D_{ex} = 0$, $d_{ex} = 0.624$). The red dots and vertical dashed lines represent the conditions, where Eqs. (2a) and (2b) are satisfied, indicating the values of κ^*. The violet dots in (a) represent the conditions, where only Eq. (2a) is satisfied.

Ref. [33], based on an analysis of the static properties of stripe domain patterns.

Figure 1 shows the dispersion relations of SWs in a film with $d_{ex} = 0.624$, an exemplary value corresponding to ultrathin Co film of $d = 2$ nm (see the Methods section) in the DE geometry for different critical parameters. Let us first consider the system with $Q = 1.1$; see Fig. 1(a). The in-plane magnetization state is forced by applying a sufficiently high in-plane bias field. The dispersion is plotted for $h = 1.06h^*$, where the critical field is $h^* = 0.123$. The dispersion for h^* has very sharp minima reaching $f = 0$ (marked with the red dots), fulfilling Eqs. (2a) and (2b). For the higher field value, the minima (marked with the violet dots) fulfill Eq. (2a) only; however, their locations κ_{min} are very close to κ^*, while their frequency is $f_{min} > 0$. The following plots in Figs. 1(b), 1(c), and 1(d) indicate conditions suitable for SRT of the other types for $Q < 1$. We start from the same set of parameters, i.e., $h = 0$, $Q = 0.6$, $D_{ex} = 0$, and $d_{ex} = 0.624$; the corresponding dispersion curve is represented by the black line in each plot. To obtain $f(\kappa^*) = 0$, we need to increase the following: (i) Q to $Q^* = 0.977$, or (ii) D_{ex} to $D_{ex}^* = 0.87$, or (iii) d_{ex} to $d_{ex}^* = 4.87$; the respective curves are plotted with the red lines in Figs. 1(b), 1(c), and 1(d).

In Appendix E there is an analysis revealing that for small field values, the global minimum of dispersion dependence falls for DE modes (see Fig. 11). It occurs even when the backward volume modes corresponding to the propagation along the field direction have significantly lower frequencies at high fields. As h^* is approaching, the minimum of the DE dispersion drastically drops down below the bottom of the backward mode band around κ^*. This observation confirms

our assumption of the unique relationship between DE SWs and SRT.

III. ANALYSIS OF PHASE TRANSITIONS

The analytical dispersion relations presented above describe the SW dynamics in uniformly in-plane magnetized films in the linear approximation. Let us analyze the results of micromagnetic simulations performed with MuMax3 software [37] to better understand the nature of the instability while approaching $f = 0$. In principle, any of the above-discussed SRT scenarios could be considered for demonstration; however, we focus our discussion on the H-SRT, which is the simplest to realize experimentally. Thus, we select h as the free parameter, keeping constant Q, D_{ex}, and d_{ex}. We will approach h^* for the following two systems: (a) ultrathin film ($d_{ex} < 1$) with $Q > 1$, focusing our discussion on a 2-nm-thick Co layer ($d_{ex} = 0.624$), and (b) thin film with $Q < 1$, considering a 200-nm-thick film of yttrium iron garnet (YIG) ($d_{ex} = 11.9$). The details of simulations are specified in the Methods section.

A. Ultrathin films

We perform micromagnetic simulations of an ultrathin film, discussed in Fig. 1(a). First, we analyze the field-dependent response of a uniformly magnetized film to a point-source-like low-amplitude excitation that can be treated as local fluctuations enabling broadband excitation of SWs. For several values of $h > h^*$, we simulated the SW dispersion relation, which in addition to revealing the frequency dependence on the wave number [Eq. (1)], also indicates the relative intensity of SWs (see Fig. 7 in Appendix B for sample plots). The SW intensity reaches a maximum at the bottom of the SW spectrum (κ_{min}, f_{min}), and increases drastically when h decreases to h^*, as presented with the empty-square line in Fig. 2(a). Our analysis indicates the linearization of the SW polarization along the z-axis and the way of entering the nonlinear regime just before the SRT. This indicates a significant enhancement of the susceptibility of the soft SW mode when approaching the SRT in accordance with predictions made for other hydrodynamic systems [2]. For each calculated dispersion, we also take the wavelength $\Lambda_{ex}^{min} = 2\pi d_{ex}/\kappa_{min}$ related to the minimum of $f(\kappa)$ dependence. In Fig. 2(b), the numerical results (open squares) superimposed with the theoretical predictions obtained from Eq. (1) (dotted line) are shown, revealing a very good agreement. While decreasing h down to h^*, the SW wavelength decreases slightly and approaches the critical value Λ_{ex}^*.

In the same system, we analyze the static magnetization distribution for $0 < h < h^*$. We determine the field-dependent magnetic configuration, for which the energy density of the system reaches the minimum. While increasing h, the mean values of normalized m_y and squared m_z magnetization components, $\langle m_y \rangle$ and $\langle m_z^2 \rangle$, respectively, increase to 1 and decrease to 0, respectively, reaching the SRT [Fig. 2(a)], whose location (field value) is in a very good agreement with the theoretical one [Fig. 1(a)]. Figure 2(b) shows the field dependence of the stripe domain period p_{ex}. One can find that
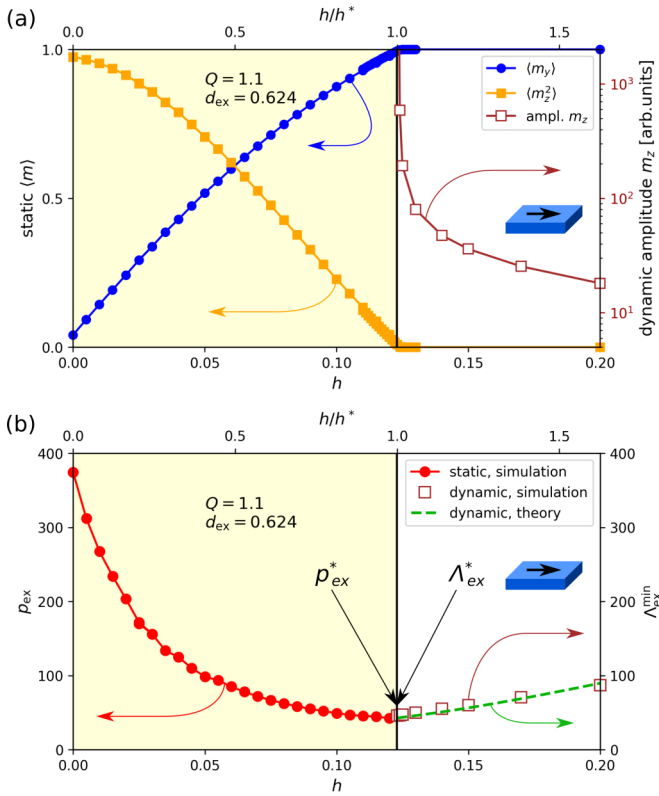
FIG. 2. A relation between the static magnetization configuration of a stripe domain pattern and the SW profile, below and above the SRT, respectively. Simulations have been performed for an ultrathin film depending on h for $d_{ex} = 0.624$, $Q = 1.1$, and $D_{ex} = 0$. Normalized field h-dependencies are of the following: (a) static $\langle m_y \rangle$ and $\langle m_z^2 \rangle$ (solid circles and squares); critical field $h^* = 0.123$ is determined by simulations; maximal amplitude of m_z oscillations from dynamic simulations (open squares); (b) reduced equilibrium domain period p_{ex} from static simulations (solid circles), SW wavelength Λ_{ex}^{min} from dynamic simulations (open squares), and from theory given by Eqs. (1) and (2a) (dashed green line). Solid lines are plotted as guides for the eye. The yellow background corresponds to the field range of occurrence of a magnetic state with an out-of-plane magnetization component, and the white background corresponds to an in-plane state.

the critical p_{ex}^* is equal to the critical Λ_{ex}^*, and that p_{ex}^* has an order of magnitude lower value than p_{ex} at remanence.

Matching of Λ_{ex}^* and p_{ex}^* is an important result demonstrating a direct connection between the SWs just above h^* and the stable magnetization configuration just below h^*, despite their very different mechanisms: the low-amplitude linear dynamics of propagating excitation prove to be correlated with the static magnetization distribution after the SRT, a nonlinear process by its very nature. This correlation is illustrated by temporal evolution of the magnetization distribution from the uniform in-plane state after the point-source-like excitation (see the Methods section) in the vicinity of h^*. For $h \lesssim h^*$ [Fig. 3(a)], the SW spreads with increasing amplitude and finally stabilizes after a few nanoseconds as a periodic stripe domain pattern, covering the whole area of the simulated film. In contrast, for $h \gtrsim h^*$ [Fig. 3(b)], only low-amplitude SWs occur, spreading from the source and decaying over

time due to damping. The temporal profiles of $\langle m_z^2 \rangle$ (averaged over the whole sample) for $h \lesssim h^*$ and $h \gtrsim h^*$ are superimposed in Fig. 3(d) as black and blue lines, respectively. They clearly indicate a nonlinear process of spontaneous spatial-symmetry breaking initiated by low-amplitude disturbance of magnetization; for h^*, where $f = 0$, that disturbance is frozen, yielding the formation of a domain pattern of the same period. Therefore, mode softening for fields below h^* leads to the formation of the stripe domain pattern, i.e., SW freezing.

The introduction of DMI to our systems leads to an intriguing effect of formation of the time-dependent phase of magnetization with a flowing stripe domain pattern [5,6]. Temporal evolution of the magnetization profile for the system with $D_{ex} \neq 0$ is shown in Fig. 3(c). The magnetic field is slightly below h^* to enable pattern formation. The DMI results in pattern flowing in the direction determined by the sign of κ^*. The amplitude of excited magnetization increases to saturation [Fig. 3(d)], and the flowing patterns slow down and stabilize. This structure may be considered as another possible realization of the room-temperature space-time crystals [38–40]. We observe that the completion time of the SRT is significantly longer with the DMI, and strongly decreases with increasing damping constant α. This is clearly visible in Fig. 3(d); cf. the dashed orange and dashed red lines corresponding to $\alpha = 0.005$ and 0.02, respectively. In the latter case, it takes 70 ns from the initiation of the fluctuation to stabilize the resulting magnetic distribution fully, while for lower α the stabilization process is several times slower. The SW freezing process for both $D_{ex} \neq 0$ and $D_{ex} = 0$ cases is additionally illustrated in dynamic plots within the movie, provided in the Supplemental Material [41].

Here, it is significant that for both cases $h < h^*$ shown in Figs. 3(a) and 3(c), during the SRT we observe an expansion of a periodic magnetization distribution with an increasing range of angles of deviation from the initial in-plane orientation. This behavior is very different from that of SWs, whose amplitude, due to damping, usually decreases rapidly with time. This type of expansion of the magnetic distribution occurring during SRT, in systems with DMI and a flowing pattern, can move for long distances, and the damping is no longer a limiting factor, but it influences the rate of the amplitude increase. These patterns may find various applications and provide a playground for fundamental studies of phase transitions in space and time. For example, in addition to using a continuous drive that results in a Floquet time crystal, a pulse technique can be used where a time crystal is initiated by a drive that is turned off [42]. This scenario is illustrated in Fig. 3(c), where a *sinc*-type pulse of the microwave field initiates the emergence of the dynamic flowing magnetization pattern.

B. Thin films

Within the already discussed ultrathin case, the magnetization distribution has been homogeneous across the film thickness. At the next step, we perform a similar analysis for thicker layers ($d_{ex} = 11.9$, $Q = 0.25$), where one can expect that demagnetization induces inhomogeneous flux-closure magnetic distribution across the film thickness, such as, e.g., weak stripe domains [7,43]. For this type of stripe
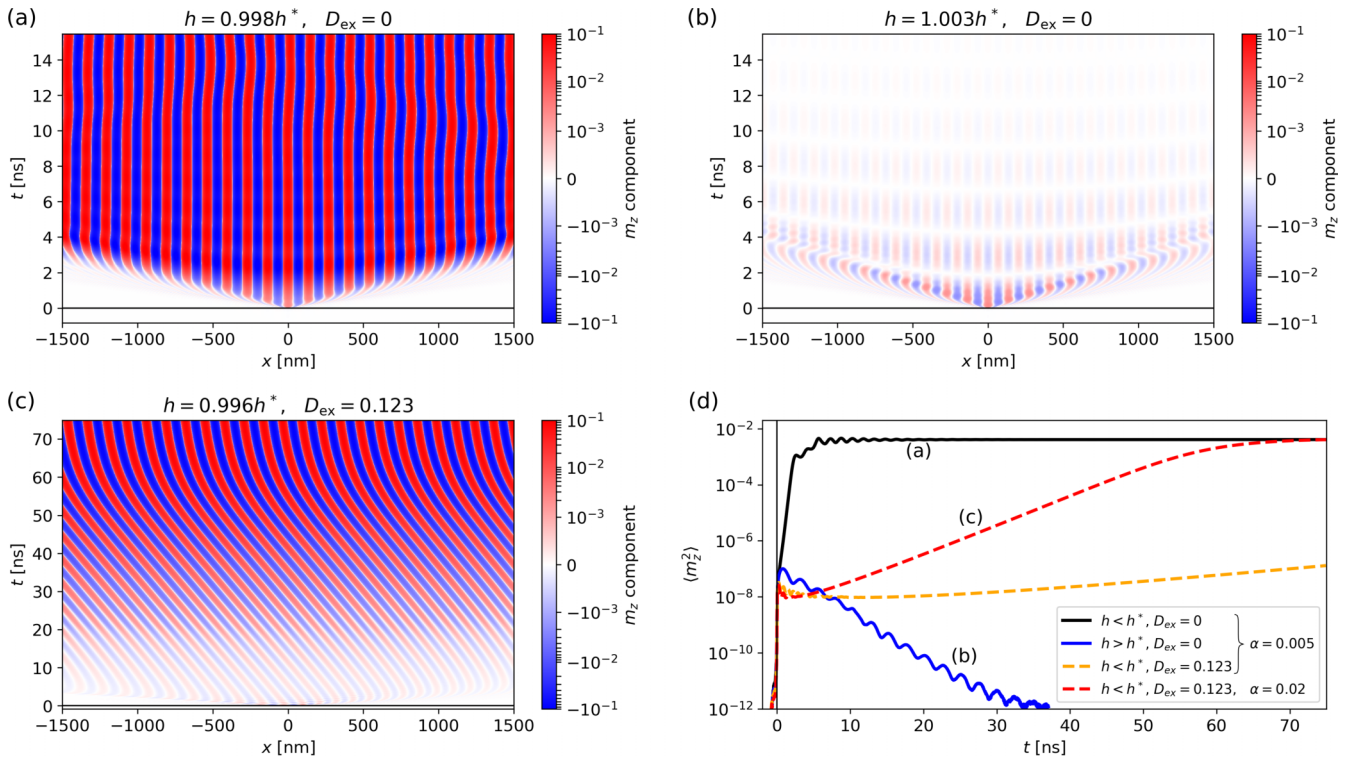
FIG. 3. Time evolution of the pattern formation in ultrathin Co film for $Q = 1.1$. (a) $h = 0.998h^*$ and (b) $h = 1.003h^*$; in these simulations, $h^* = 0.123$, $D_{ex} = 0$, and damping parameter $\alpha = 0.005$. (c) $D_{ex} = 0.123$, $h = 0.996h^*$ (where $h^* = 0.124$), and $\alpha = 0.02$. The color scales in all density maps are conserved. (d) Temporal dependencies of $\langle m_z^2 \rangle$ are averaged over the whole systems, for the cases (a), (b), and (c), and additionally for the DMI case from (c) with low $\alpha = 0.005$ (the orange dashed line). The same results in the form of a movie can be found in the Supplemental Material [41].

domains, the cross-sectional view reveals that domain walls resemble vortices with parallel in-plane aligned cores. The field dependencies in dynamics and statics, obtained from micromagnetic simulations, are qualitatively similar to those shown in Fig. 2, and they are presented in Appendix C (see Fig. 8). The dispersion relation calculated for a saturated system ($h = 1.05h^*$) is shown in Fig. 4(a). The band that approaches $f = 0$ at $\kappa = \kappa^*$ is responsible for the phase transition. The maximum of magnetization dynamic amplitude is observed at (κ_{min}, f_{min}) at the minimum of SW dispersion, as marked by the black dot. The cross-sectional view of the SW amplitude distribution at this point is shown in Fig. 4(b). The
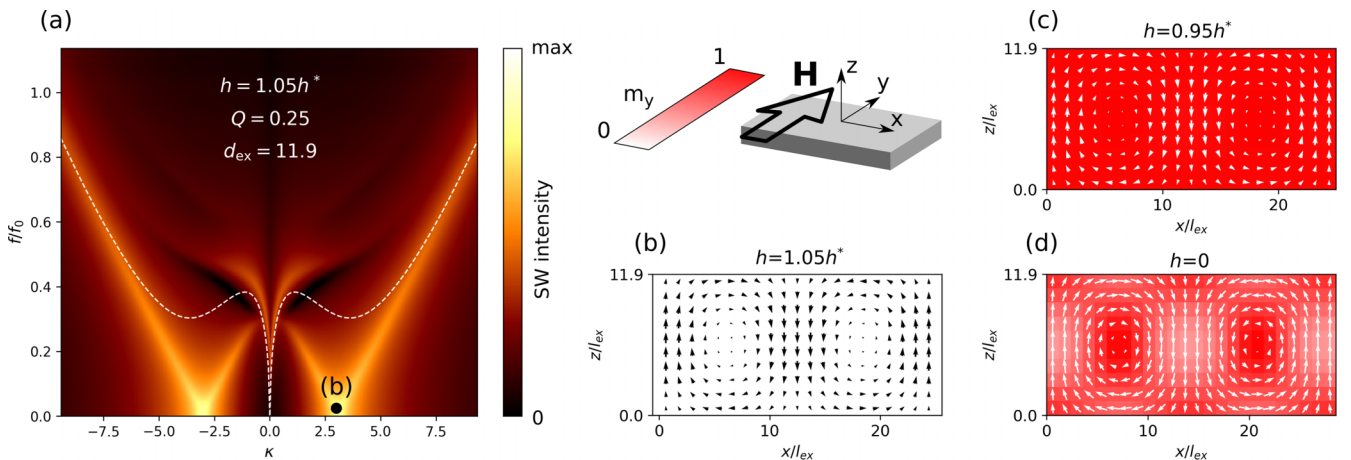

FIG. 4. Simulated h-dependent static and dynamic properties of thin film with $Q = 0.25$, $D_{ex} = 0$, and $d_{ex} = 11.9$. (a) SW dispersion relation for $h = 1.05h^*$ (SW intensity is in log scale); the white dashed line represents the analytical dispersion [Eq. (1)]; (b) mode of oscillations at the point (κ_{min}, f_{min}) in the dispersion relation, as marked with the black dot in (a); the m_x and m_z dynamic magnetization components are presented by the black arrows, $m_y \approx 1$; (c),(d) static magnetization distribution at $h = 0.95h^*$ and 0, respectively. The m_x and m_z static magnetization components are presented by the white arrows, while the static m_y component is coded by color.

profile should be understood as a *photograph* of distribution of the dynamic magnetization component, moving along the x direction. This dynamic magnetization distribution is similar to the static magnetization weak stripe domain pattern [7], found for $h < h^*$, as presented in Fig. 4(c) for $h = 0.95h^*$. Thus, the mechanism of SW freezing in thin films, regardless of the appearance of more complicated magnetic patterns, looks similar to the one discussed for ultrathin films with one-dimensional magnetization distribution. The lower the field value, the lower the phase velocity, and, finally, the phase velocity vanishes, when $f = 0$ for h^* and κ^*. At this point, we observe the SRT and finally get a weak stripe domain pattern with the spatial distribution resembling the mode profile of SWs for fields just above h^* at $\kappa \approx \kappa^*$. While decreasing the field down to 0, this flux closure vortex-type structure [Fig. 4(d)] evolves: m_x and m_z magnetization components become more distinct, and the domain period increases slightly. The theoretical dispersion relation [Eq. (1)] plotted in Fig. 4(a) with the white dashed line cannot be used to find conditions required for the occurrence of SW freezing in thin film since it does not describe SW dynamics well in thicker films. Numerical simulations more accurately describe the properties of such systems.

IV. INFLUENCE OF H, Q, D, AND d ON THE SRT

We already know that the SW softening mediates a phase transition from the in-plane saturated state to the stripe domain pattern with a period matching the wavelength of SWs at zero frequency. We discussed the H-SRT case, and now let us analyze the other types of SRTs, which can be understood as boundaries in a multidimensional space of material parameters, h, Q, D_{ex}, and d_{ex}. Below we discuss SRTs on the following two planes: (a) (Q, D_{ex}) and (b) (Q, d_{ex}).

A. SRTs on the (Q, D_{ex}) plane

To characterize the SRT within the (Q, D_{ex}) cross-section of the available parameter space, in the case of ultrathin films (here, we take $d_{\text{ex}} = 0.624$), one can solve Eqs. (2) numerically. The results of such calculations are shown in Figs. 5(a) and 5(b). The white region corresponds to the in-plane magnetization state, and the yellow-red regions correspond to the states with a nonzero out-of-plane magnetization component. The separating solid black line marks the zero-field SRT, and it can also be calculated analytically [see Eqs. (A1) in Appendix A]. Within the out-of-plane state, the magnetization can be turned into an in-plane orientation if the bias field is above the critical field h^* plotted as contours in Fig. 5(a). The critical field value is found to be increasing with both Q and D_{ex}. The values of Λ^*_{ex} (or p^*_{ex} equivalently) plotted as contours in Fig. 5(b) generally decrease with increasing D_{ex}, with a minor dependence on Q. They can be compared with the calculated equilibrium domain structure period p_{ex}, corresponding to the minimal energy state in the zero external magnetic field shown in Fig. 5(c). An analogical map of the equilibrium period plotted for a Co film with a different thickness and a variety of possible magnetic states are discussed in Ref. [34]. There is a substantial difference in values of domain periods, critical p^*_{ex} and p_{ex} at remanence,

in particular in the right-bottom corner of the diagram, where the latter one can be orders of magnitude higher [33]. In fact, this diversity has already been discussed in Sec. III A and illustrated for the case $D_{\text{ex}} = 0$ in Fig. 2(b). On the other hand, both periods are converged in the top part of the diagrams (for high D_{ex}). Figure 5(d) shows scans of p^*_{ex} and p_{ex} along D_{ex} for selected values of Q. This demonstrates a possibility of the existence of a stripe domain varying widely in size, depending on the magnetic history. When operating with the perpendicular field, huge equilibrium domains may be formed. On the other hand, when playing with the in-plane field, fine structure can be obtained at the H-SRT from the frozen SW, and this structure should persist as metastable even after reducing the field down to 0. The possibility of the formation of domains of hugely different sizes using a perpendicular or in-plane applied magnetic field has been confirmed experimentally in Co ultrathin films [32]. Another example of diversity of magnetization states depending on sample magnetic history is the domain structure formation across temperature-driven SRT due to reversible $Q(T)$ dependence [44].

B. SRTs on the (Q, d_{ex}) plane

Another view of the phase transition diagram in our four-dimensional parameter space is provided in Fig. 6, showing the Q and d_{ex} dependencies with constant $D_{\text{ex}} = 0$, with a similar (to Fig. 5) convention of colors for the ranges of the in-plane and out-of-plane magnetization distributions. The solid black lines in Fig. 6 describe the zero-field SRT constructed by the classical approach proposed by Hubert [7,45] and based on micromagnetic equations considering domain nucleation. Characteristic regimes in the (Q, d_{ex}) space can be distinguished. In ultrathin films ($d_{\text{ex}} < 1$), the parameters h^* and Λ^*_{ex} can be described analytically with Eqs. (3) [or higher-term approximation-based Eqs. (D1)]. For these equations, as well as for numerical solution of Eqs. (2), the zero-field SRTs are plotted in Fig. 6(b) with the dashed lines. While leaving the ultrathin regime (increasing d_{ex}), the minimum of SW dispersion for a field approaching the critical field h^* (SW freezing effect) should be determined numerically due to discrepancies in this regime for the analytical dispersion relation based on Eq. (1). This is discussed above and illustrated in Figs. 4 and 9. Finally, the regime of low Q and high d_{ex} media can be described analytically again with Eqs. (D2), applied after Ref. [25], discussed further in Appendix D. The contours in Figs. 6(a) and 6(b) are the values of h^* and p^*_{ex} (or equivalently Λ^*_{ex} of the softened SWs), respectively, calculated with micromagnetic simulations of the magnetization state over wide ranges of Q and d_{ex}. The bottom parts of both maps (low d_{ex} below the *scissors*) are calculated using the theoretical approach [Eqs. (D1a) and (D1c)]. Interestingly, p^*_{ex} or Λ^*_{ex} changes in a nonmonotonic way, reaching higher values at either $d_{\text{ex}} \ll 1$ or $Q \ll 1$ regions. In the inset to Fig. 6(b), we present the simulated behavior of $p^*_{\text{ex}}(d_{\text{ex}})$ along the $h = 0$ SRT line assisted with the theoretical dependencies and plotted for analytically describable regimes. Speaking in terms of κ, inversely proportional to the wavelength (or period), the low κ regions (or high Λ_{ex} or p_{ex} regions at either low d_{ex} or low Q) have a particular practical experimental importance. In those regimes, it is possible to excite SWs by experimentally
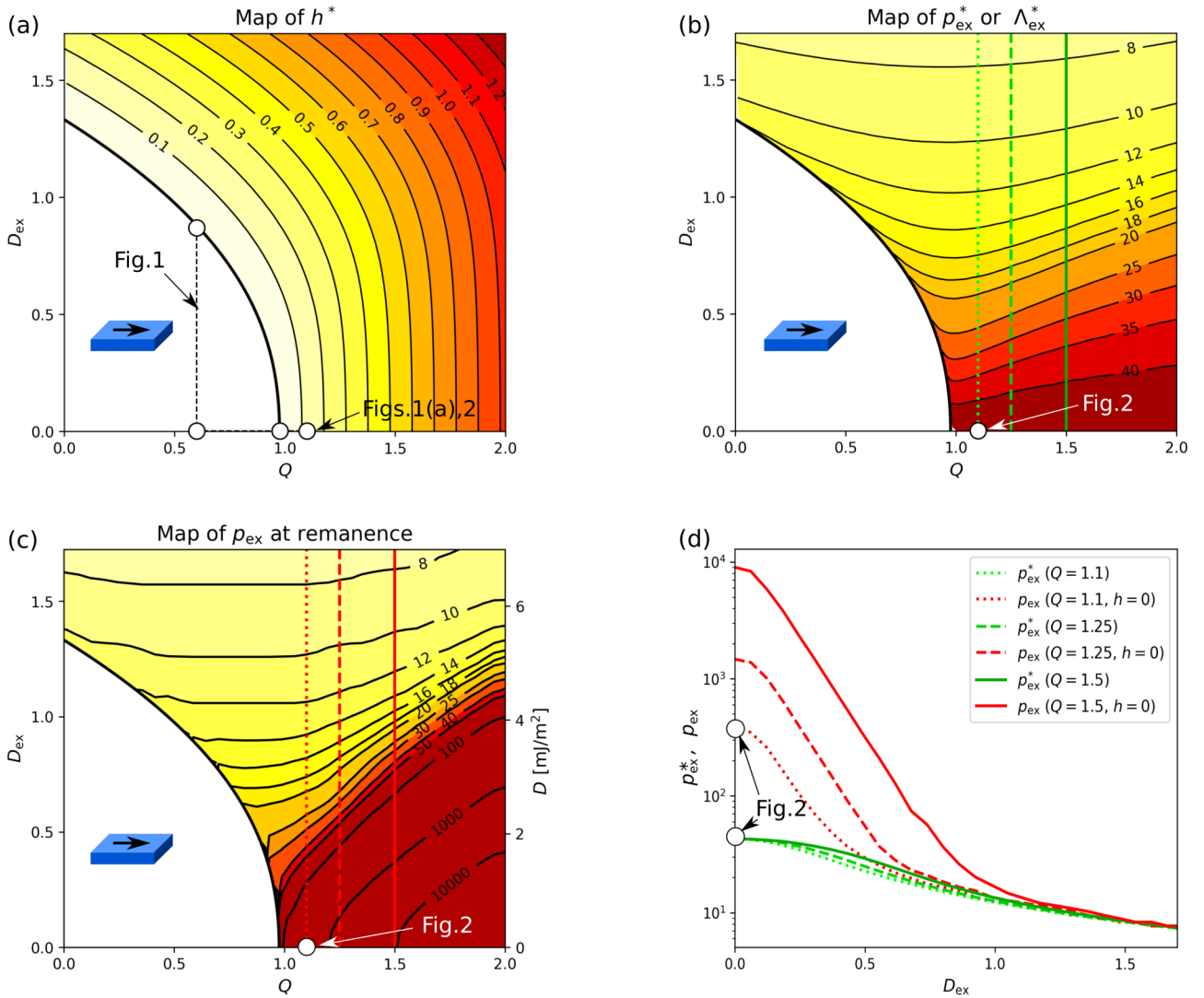
FIG. 5. Calculated diagrams and SRT lines in the (Q, D_{ex}) space for the ultrathin film case with $d_{ex} = 0.624$. (a),(b) Theoretical SRT [i.e., numerical solution of Eqs. (2a) and (2b)]; (a) the map of critical field h^*; (b) the map of critical period p^*_{ex} or wavelength Λ^*_{ex} for the values of h^* shown in (a); (c) the map of reduced period found in micromagnetic simulations from energy minimization at zero field; (d) a comparison of freezing (b) and zero-field (c) reduced periods for selected Q values [marked with the vertical lines in (b) and (c)]. The white points denote the parameters discussed in the labeled figures.

available antennas, or to detect SWs by the Brillouin light scattering (BLS) technique [25] instead of large-scale facility synchrotron methods [46] required for studying the high κ (small Λ_{ex} or p_{ex}) regime. For SW excitations at $h > h^*$, the values of interesting κ (or Λ_{ex}) do not change substantially, as can be noted in Figs. 2(b) and 8(b).

The open symbols in Fig. 6(a) represent the values of (Q, d_{ex}) already discussed throughout the manuscript and presented in the labeled figures. Within the open triangle, we also considered a point in the $Q \ll 1$ regime where the analytical formulas [Eqs. (D2)] can be used. In Fig. 11 in Appendix E, we discuss the simulated spectra in the DE configuration for two field values, illustrating the effect of SW freezing. The obtained values of critical parameters are in good agreement with the analytical ones. Additionally, for the identical parameters, we calculate the spectra in the backward-volume magnetostatic wave geometry. Different minima for these

modes clearly indicate that SW freezing takes place for the DE mode that is connected to the creation of stripe domains along the magnetic field.

Finally, let us discuss the advantages of using the nondimensional parameters introduced in the dispersion relation [Eq. (1)] and exploited throughout this work. Any given set of parameters h, Q, D_{ex}, and d_{ex} can be recalculated for different material, involving different material-specific M_s, A_{ex}, and gyromagnetic ratio γ, and yielding the same effect for proper absolute parameters H, K_u, D, and d. This issue is discussed in detail in Appendix F. Our nondimensional space covers a number of magnetic materials with a broad range of accessible parameters depending on the experimental goal and taking into account the limitations of available experimental methods. For example, l_{ex} in YIG is about five times larger than in Co due to different M_s and A_{ex} values; thus, about five times larger real thicknesses and, in dynamics, about
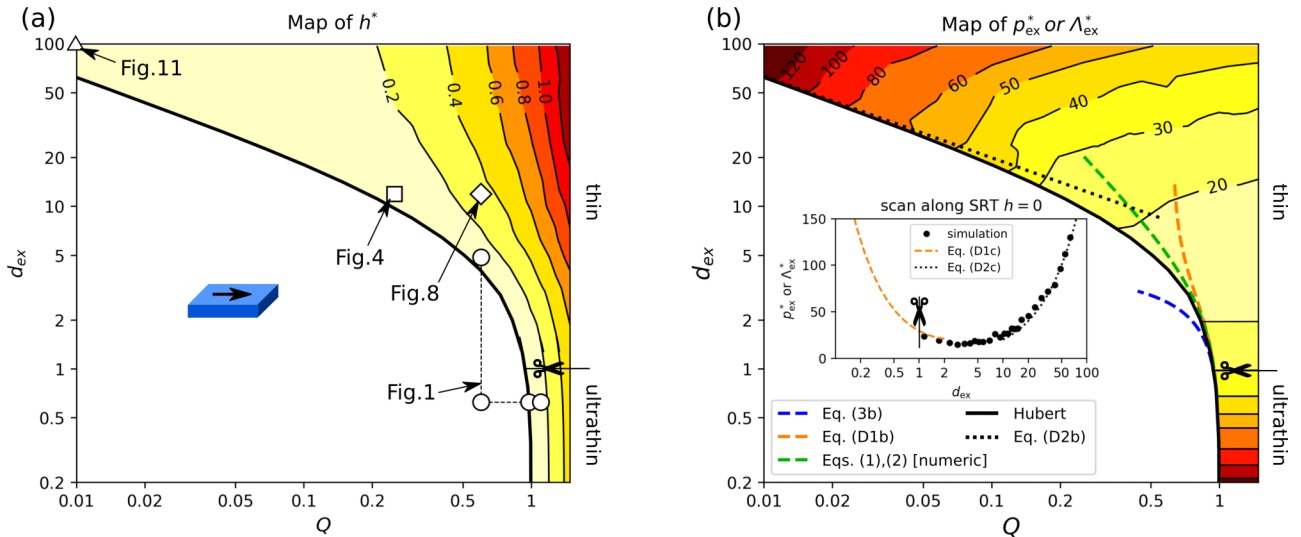
FIG. 6. Simulated SRT in the (Q, d_{ex}) space for $D_{ex} = 0$. (a) The map of critical field h^*; (b) the map of critical period p_{ex}^* or wavelength Λ_{ex}^* for the values of h^* shown in (a). The open symbols in (a) denote the values of parameters discussed throughout the manuscript and presented in the indicated figures. The dashed lines in (b) are analytical and numerical approximations of zero-field SRT according to the dispersion-based theory, and the dotted line is the zero-field SRT in the $Q \ll 1$ regime. The black solid line in (a) and (b) is Hubert's theory for the zero-field SRT. The area below the scissors is filled according to theoretical dependences instead of simulations (see the text for details). The inset in (b) is a scan of p_{ex}^* or Λ_{ex}^* along the zero-field SRT (the black "Hubert" line) according to simulations and applicable analytical approaches.

five times lower wave numbers are required for the same effect to occur in YIG. In particular, large wave numbers can be a bottleneck in experimental validation, e.g., in BLS, where the employed laser light wavelength limits the SW wave numbers, resulting in measurable periods in the range of hundreds of nanometers. On the other hand, frequencies that scale with M_s, are about 10 times lower in YIG than in Co. Recently, DMI has been proven to exist also in garnets [47], and although the absolute D values in these materials seem to be extremely low as compared to those found in metals, the values of the corresponding reduced parameter D_{ex} are similar. The results of micromagnetic simulations indicate that the normalized parameters work well up to the instability for ultrathin and thin films. It is important to note that based on the normalized parameters in the linear SW theory, we can estimate the magnetization stripe domain pattern emerging in a nonlinear remagnetization process due to the demonstrated correlation between the softening of SWs and the nucleation of stripe domains.

V. CONCLUSIONS

We have provided a combined view of the interplay between static stripe magnetic domains and the SW dynamics in films with uniaxial perpendicular magnetic anisotropy and DMI, representing an important class of ferromagnetic materials. The interconnection involves a critical behavior of SWs, with the vanishing of their phase and group velocities at a critical value of the bias magnetic field, which is accomplished by the DE type of SWs, regardless of which type of mode has the minimum at higher magnetic field values. At the critical field, the SW freezes, its amplitude rises, and a stripe domain

structure is formed with the period p_{ex}^* and spatial distribution equal to the wavelength Λ_{ex}^* and profile, respectively, of the frozen SW. From the static point of view, this occurs in the form of an SRT.

Our study is based on an analytical approach and micromagnetic simulations with analysis of the bias magnetic-field-induced transition H-SRT, the most common and very significant one for its reversibility. However, the freezing process is also observed in other transitions, such as Q-SRT or D-SRT, which can also be realized reversibly by changing the temperature or the electric field. The thickness-driven phase transition d-SRT is related to following different magnetization distributions: simple stripe domains in ultrathin films, and complex weak stripe domains that are nonuniform across thickness, with domain walls resembling vortices in thicker films with $Q < 1$, and asymmetric across the film thickness when $D \neq 0$. At remanence, the creation of different domain structures can be expected, as follows: (i) metastable structures with the critical period p_{ex}^*, and (ii) equilibrium structures with a period up to orders of magnitude larger than p_{ex}^*. p_{ex}^* can be described with simple analytical formulas either in low-d_{ex} or in low-Q approximations. We have shown that the formation of the stripe magnetic domain in homogeneously magnetized ferromagnetic film can be induced by a pulselike point source of SWs just below SRT, offering a scenario for the expansion of the magnetization pattern at velocities controlled by damping.

The DMI breaks time-reversal symmetry in ferromagnetic ultrathin films, but it also results in the formation of a flowing stripe domain magnetization pattern after passing through an H-SRT with a decreasing bias magnetic field. This effect can offer an opportunity to form magnonic space-time crystals

and study fundamental properties of classical systems related to spontaneous translational symmetry breaking in space and time.

Our simulations have been performed for ultrathin and thin films of cobalt and yttrium iron garnet. However, the results presented in the units normalized to the material constants can be easily rescaled to other magnetic media with the extension of the conclusions made.

VI. METHODS

We used MuMax3 [37] to perform micromagnetic simulations for the following two representative systems: (i) a 2-nm-thick Co ultrathin film with $M_s = 1.42$ MA/m and $A_{ex} = 13$ pJ/m, and (ii) a 200-nm-thick YIG thin film with $M_s = 143$ kA/m and $A_{ex} = 3.65$ pJ/m. The assumed values of M_s and A_{ex} in the Co and YIG films correspond to the exchange lengths of 3.2 and 16.8 nm, respectively; thus, the reduced thickness values in the respective systems are $d_{ex} = 0.624$ and 11.9. The sizes of the simulated systems are $S_x \times 10 \times 2$ nm^3 and $S_x \times 100 \times 200$ nm^3, and those of their unit cells are $1 \times 10 \times 2$ nm^3 and $10 \times 100 \times 10$ nm^3, respectively. In simulations, we assume the periodic boundary conditions along the x and y directions; therefore, we can regard our system as infinite in the (x, y) plane. Static relaxation of the systems has been performed to determine the preferred magnetization orientation and the domain stripe period in the out-of-plane magnetization state. The value of S_x has been adjusted for different H, Q, and D values, and the total energy density of the sample has been monitored to find the minimal energy state. In addition to the two basic systems of the described geometries, different films thicknesses have also been simulated for Co film by increasing the number of cells along the z direction, keeping the unit cell size constant.

The dynamic response of the system has been calculated after a low-amplitude localized microwave magnetic field pulse, sinc-shaped in the spatial and temporal domains, $h_{mf} = a \, \text{sinc}(2\pi f_{cut} t) \text{sinc}(k_{cut} x)$, applied along the $(1, 1, 1)$ direction, with the peak-amplitude a of order of 0.1 mT, and various cutoff frequencies f_{cut} and cutoff wave numbers k_{cut}, selected individually to cover a region of interest of particular dispersion relations (see the maximal values of f and k in the presented dispersions). The simulation started at $t = -10/f_{cut}$. The calculations have been done for Gilbert damping constant $\alpha = 0.05$ (or lower if specified) and for gyromagnetic ratio $\gamma = 1.76 \times 10^{11}$ rad/T/s. The dispersion relations for the data stored with the sampling interval providing spectral resolution up to $f_{max} = 1.1 f_{cut}$ have been calculated by the two-dimensional fast Fourier transformation (FFT) of a time-dependent stack of x-dependent magnetization distributions (m_z component, averaged over the thickness), converting a 2D (x, t)-dependent matrix into reciprocal space (k, f). The mode profiles have been calculated using the inverse FFT from the (k, f) space with a binary mask composed of 1 in a selected point (k_0, f_0) and 0 elsewhere. In this case, both m_x and m_z components were taken into account, keeping the resolution along the z direction.

APPENDIX A: SW SOFTENING IN ULTRATHIN FILMS WITH DMI

In Eqs. (3) in the main text, the formulas for critical parameters at the SRTs have been proposed for the ultrathin case, without DMI. Under the same approximation of $\xi(\kappa) = |\kappa|/2$, the conditions (2) and (1) can also be found for $D_{ex} \neq 0$. For the simple case of the zero-field SRT, the equations can be solved analytically, yielding

$$Q^* = 1 - \frac{3a}{8} + \frac{3a^2}{16d_{ex}^2} + \frac{5d_{ex}^2}{16} - \frac{3d_{ex}^4}{8a} + \frac{3d_{ex}^6}{16a^2} - D_{ex}^2,$$

(A1a)

where

$$a = \sqrt[3]{d_{ex}^4 \left(2D_{ex} + \sqrt{d_{ex}^2 + 4D_{ex}^2}\right)^2}.$$

(A1b)

The critical SW wavelength is

$$\Lambda_{ex}^* = p_{ex}^* = \frac{4a}{a^2 - a d_{ex}^2 + d_{ex}^4},$$

(A1c)

which is far more complicated than the respective Eqs. (3). Nevertheless, the formulas for Q^* and Λ_{ex}^* from both sets of equations become identical, when inserting $D_{ex} = 0$. Equation (A1a) is plotted for $d_{ex} = 0.624$ in Figs. 5(a) and 5(b) in the main text, and it agrees well with the boundary $h = 0$ SRT found from numerical calculations for the original $\xi(\kappa)$ (without approximations).

APPENDIX B: DISPERSION RELATION IN ULTRATHIN FILMS

The dynamic response of a uniformly magnetized ultrathin film with $d_{ex} = 0.624$ (i.e., a Co film with $d = 2$ nm) and $Q = 1.1$ has been simulated for several values of $h > h^*$; the results are shown in Fig. 2 and discussed in the main text. The simulated dispersion relations are presented in Fig. 7, where they are compared with the theoretical predictions based on Eq. (1), represented by black dashed lines. The case considered in Fig. 7(b) is the same as that in Fig. 1(a) in the main
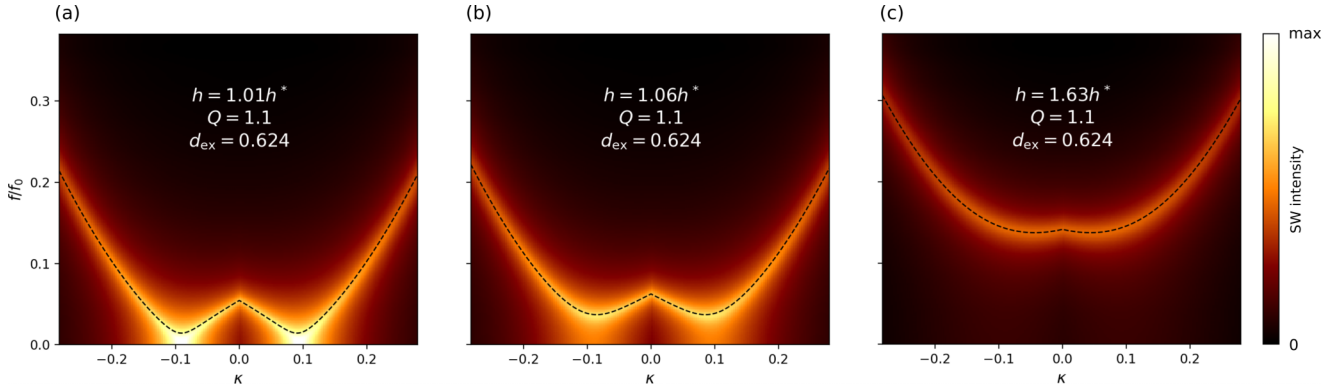
FIG. 7. Dispersion relation in ultrathin film for $d_{ex} = 0.624$ (i.e., 2 nm of Co), $Q = 1.1$, $D_{ex} = 0$, and increasing field, all above the critical value $h^* = 0.123$: (a) $h = 1.01h^*$; (b) $h = 1.06h^*$ [this is the case presented in Fig. 1(a)]; 1(c) $h = 1.63h^*$. SW intensity is coded by color in log scale. While increasing the field, the band moves up and its intensity decreases. The dashed lines are plotted according to the dispersion-based theory [Eq. (1)].

text. With increasing field, the observed band moves up and its intensity near the minima decreases, as explained in Fig. 2(a).

APPENDIX C: SW FREEZING AND DISPERSION RELATION IN THIN FILMS

The orientation of the static magnetization in thin film $d_{ex} = 11.9$ (which corresponds to 200 nm of YIG) and $Q = 0.25$ has been calculated versus h to determine the value of h^*, as has been done for the ultrathin film (Fig. 2 in the main text). Note that these results are qualitatively similar. The critical field value $h^* = 0.04$ has been found from the field dependences of $\langle m_y \rangle$ and $\langle m_z^2 \rangle$. The result is presented in Fig. 8(a) along with the amplitude of the dynamic response of the system for $h > h^*$ that increases strongly as h decreases to h^*. Figure 8(b) shows the field dependence of the following: (i) reduced equilibrium (minimum energy) domain period for $h < h^*$, and (ii) SW wavelength at minimum of SW dispersion for $h > h^*$.

The dispersion relations for this thin film have been calculated for several values of Q and $h > h^*$. The selected cases are illustrated in Figs. 9(a) and 9(b) for $Q = 0.6$, in $h = 1.03h^*$ and $h = 1.21h^*$, respectively, where $h^* = 0.32$. Superimposed in the plot are the theoretical dependences calculated from Eq. (1), represented by dashed lines. Since the theory based on dispersions does not correctly describe inhomogeneous oscillations in anisotropic systems (as discussed in Sec. IV in the main text), the numerical and theoretical results differ substantially, except for very low (close to 0) or very high wave numbers. Figures 9(c) and 9(d) show the mode profiles for two different wave numbers, distinguished by the black points in Fig. 9(a). The mode profile for the lower wave number (large periodicity) in the range of wave vectors, where the simulation results agree with the theory, is characterized by the amplitude concentration at one of the layer surfaces, which is characteristic for DE modes. The latter mode profile, at the minimum of the band, is close to the SW freezing (when the field is slightly increased above h^*), and the dynamic magnetization pattern has a characteristic vortexlike shape as in Fig. 4 in the main text.
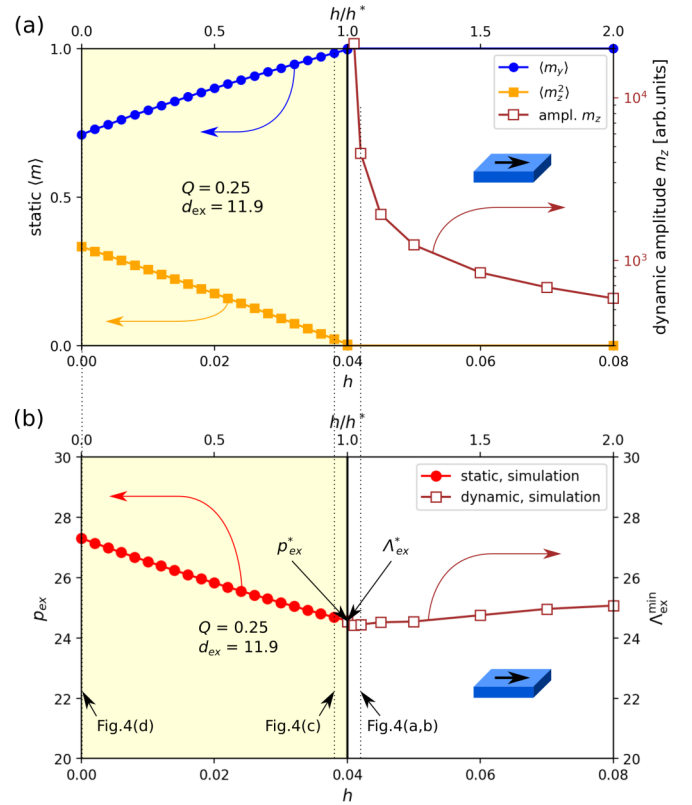

FIG. 8. A relation between the static magnetization configuration of a stripe domain pattern and the SW profile below and above the SRT, respectively. Simulations have been performed for the thin film depending on h for $d_{ex} = 11.9$, $Q = 0.25$, and $D_{ex} = 0$. Normalized field h-dependencies are of the following: (a) static $\langle m_y \rangle$ and $\langle m_z^2 \rangle$ (solid squares and circles); critical field $h^* = 0.04$ is determined by simulations; maximal amplitude of oscillations is determined by dynamic simulations (open squares); (b) reduced equilibrium domain period p_{ex} is determined by static simulations (solid circles), and wavelength of SWs Λ_{ex}^{min} is determined by dynamic simulations (open squares). Solid lines are plotted as guides for the eye. The yellow background corresponds to the field range of occurrence of a magnetic state with an out-of-plane magnetization component, while the white background corresponds to the in-plane state.
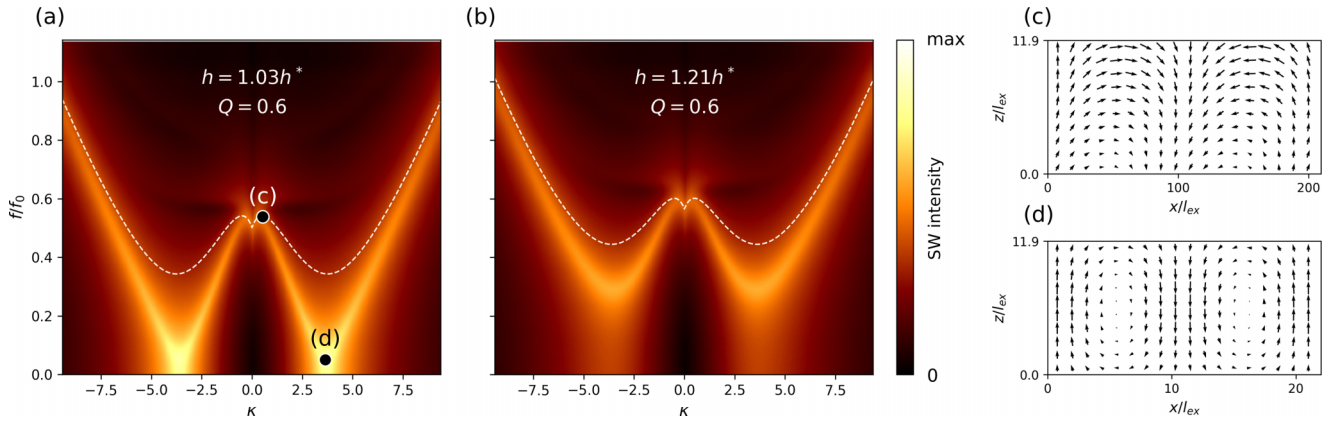
FIG. 9. Dispersion relations and SW mode profiles in thin films, $d_{ex} = 11.9$ and $Q = 0.6$. (a),(b) Dispersion relations for $h = 1.03h^*$ and $1.21h^*$. While increasing the field above, the band moves up and its intensity decreases. SW intensity is coded by color in log scale. The white dashed lines are theoretical dependences according to Eq. (1) at the given values of the field. (c),(d) Mode profiles in $h = 1.03h^*$, where $h^* = 0.32$, at the points marked with dots in (a).

The introduction of DMI makes the dispersion relations asymmetric, as shown in Fig. 1(c) in the main text. Figures 10(a) and 10(b) present the simulated dispersion in a thin film for $D_{ex} = 0.246$ and 1.23 (that correspond to $D = 1$ and 5 mJ/m^2 in Co, respectively). As h decreases to h^*, the band descends to touch the $f = 0$ axis at a negative k; only at this point is the SW freezing process possible. The sign of the wave number corresponding to $f = 0$ depends on the signs of the DMI constant and the magnetic field. The mode profiles at both minima of the band [Figs. 10(c) and 10(d)] look spatially similar. The only difference is the opposite (up/down) shifts of the centers of the vortices in the domain walls. However, the frequencies and, consequently, the phase velocities differ substantially.

The asymmetry of the dispersion increases with increasing DMI, and the difference between the SW velocities at the two minima can change drastically. In particular, when the DMI is strong enough, the dispersion relation can have one minimum only, the other being flattened, as in Fig. 10(b), where $D_{ex} = 1.23$ ($D = 5$ mJ/m^2 in Co). As in Fig. 9, the

theoretical dispersion cannot describe the systems (plotted with white dashed lines) due to inhomogeneous oscillations.

APPENDIX D: CRITICAL PERIOD IN THE (Q, d_{ex}) PLANE

In Sec. IV B in the main text, the SRT is discussed in the (Q, d_{ex}) parameter space. It can be described analytically in the two following regimes: (i) ultrathin film, $d_{ex} < 1$, where $Q \gtrsim 1$; and (ii) low anisotropy, $Q \ll 1$, for $d_{ex} \gg 1$. In the former case of homogeneously magnetized ultrathin magnetic films, one can apply the dispersion-based theory and SW softening. In Eqs. (3) in the main text, the formulas for critical parameters at the SRTs have been proposed. Alternatively, one can employ a higher-term approximation of $\xi(\kappa) \approx |\kappa|/2 - \kappa^2/6$ to obtain a higher-term approximation of critical field,

$$h^* = Q - 1 + \frac{3d_{ex}^2}{8(6 + d_{ex}^2)}. \qquad (D1a)$$

For the zero-field SRT, one has

$$Q^* = 1 - \frac{3d_{ex}^2}{8(6 + d_{ex}^2)}. \qquad (D1b)$$
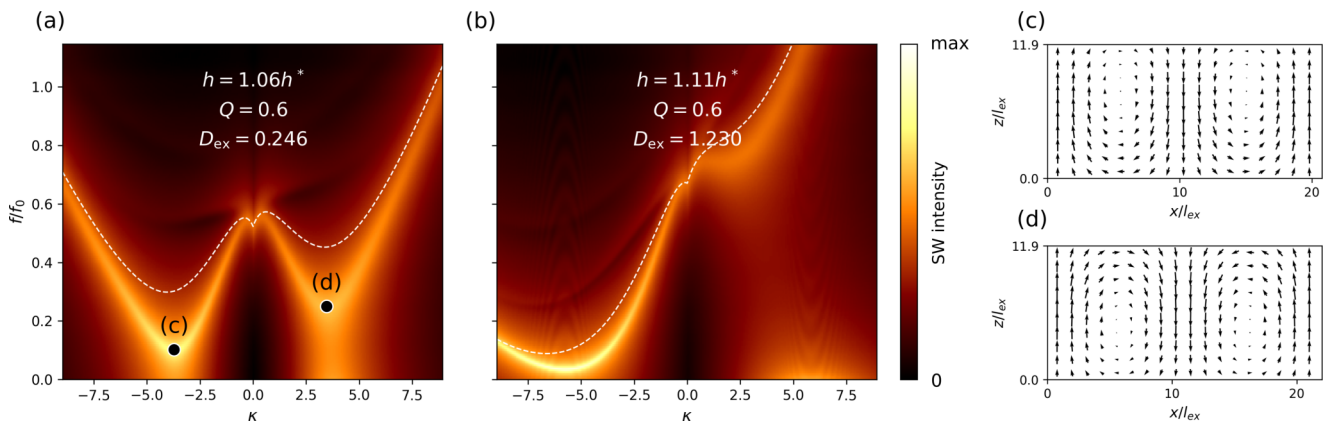
FIG. 10. Dispersion relations and SW mode profiles in thin film with DMI, $d_{ex} = 11.9$ and $Q = 0.6$. (a),(b) Dispersion relations for $D_{ex} = 0.246$ and 1.23 and $h = 1.06h^*$ and $1.11h^*$, respectively. While increasing DMI, the band tilts, becoming more asymmetric. SW intensity is coded by color in log scale. The white dashed lines are theoretical dependences according to Eq. (1) at the given values of the field. (c),(d) Mode profiles for $D_{ex} = 0.246$ in $h = 1.06h^*$, at the points marked with dots in (a).

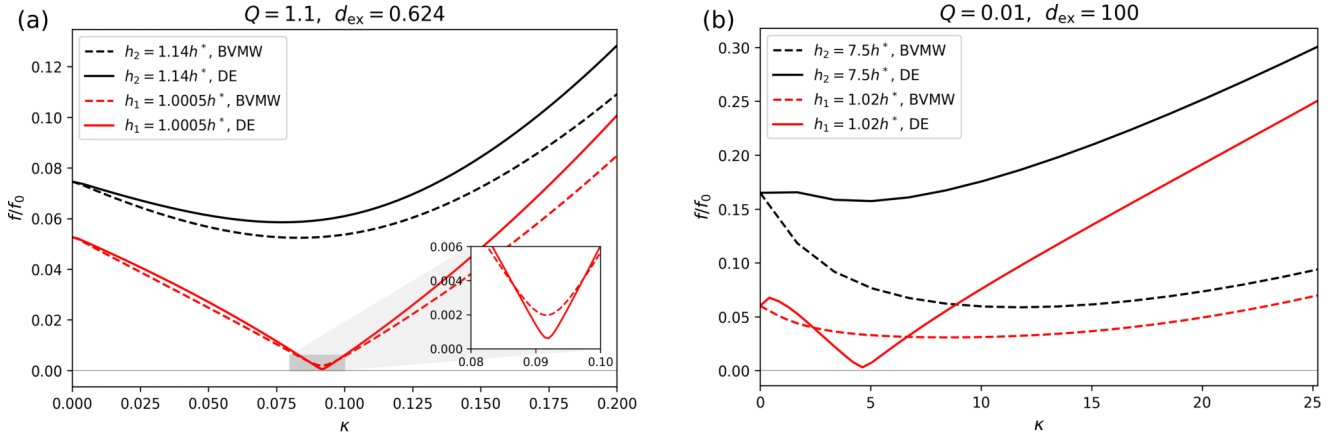FIG. 11. The simulated dispersion relations in DE (solid lines) and BVMW (dashed lines) modes for the following two systems: (a) an ultrathin film, $d_{ex} = 0.624$ and $Q = 1.1$, and in magnetic field, $h_1 = 1.0005h^*$ and $h_2 = 1.14h^*$; (b) a thick and low-anisotropy film, $Q = 0.01$ and $d_{ex} = 100$, and in magnetic field, $h_1 = 1.02h^*$ and $h_2 = 7.5h^*$.

The critical SW wavelength is

$$\Lambda_{ex}^* = p_{ex}^* = \frac{8\pi}{d_{ex}} + \frac{4\pi d_{ex}}{3}, \tag{D1c}$$

and this formula is valid for different types of SRT, being independent of h and Q. Equations (D1) become analogous to Eqs. (3) for the case $d_{ex} \ll 1$. Equations (D1a) and (D1c) are used to complete the lower part of Figs. 6(a) and 6(b), respectively, and in the inset of Fig. 6(b), as a low-d_{ex} case of $p_{ex}^*(d_{ex})$ dependence along the SRT at remanence.

On the other hand, the low-Q case is discussed in Ref. [25]. Based on the Landau theory, the authors derive an equation for critical field, which can be rewritten in our normalized units as

$$h^* = Q - \frac{2\pi\sqrt{Q}}{d_{ex}}. \tag{D2a}$$

The condition for $h = 0$ transition is then written as

$$Q^* = \left(\frac{2\pi}{d_{ex}}\right)^2, \tag{D2b}$$

which is equivalent to Hubert's theory-based approximation, and is plotted in Fig. 6(b) as the black dotted line. Further, the SW wavelength along this zero-field SRT can be calculated as

$$\Lambda_{ex}^* = p_{ex}^* = 2d_{ex}. \tag{D2c}$$

The general formula for the case $h \neq 0$ is

$$\Lambda_{ex}^* = p_{ex}^* = 2d_{ex}\sqrt{\frac{\pi}{\sqrt{Q}d_{ex} - \pi}}. \tag{D2d}$$

Between the above analytically describable regimes, the transitional middle-d_{ex} SW freezing parameters can be successfully described by micromagnetic simulations.

APPENDIX E: DE AND BACKWARD-VOLUME MAGNETOSTATIC WAVE GEOMETRIES

Let us compare the dispersion relations of SWs propagating perpendicularly and parallelly to the direction of the applied magnetic field, i.e., the DE configuration and backward-volume magnetostatic wave (BVMW) configuration, respectively. For this purpose, we performed calculations by solving the linearized Landau-Lifshitz equation in the frequency domain using the finite-element method implemented in the COMSOL MULTIPHYSICS environment [48]. We performed calculations for the following two cases: (i) ultrathin film with $d_{ex} = 0.624$ and $Q = 1.1$, and (ii) low-anisotropy media with $Q = 0.01$ and $d_{ex} = 100$ (which corresponds to 1.68-μm-thick YIG film). The results of the dispersion relations for the fields $h_1 \gtrsim h^*$ and $h_2 > h^*$ are displayed in Fig. 11 by the red and black lines, respectively. Relevant values of h^* have been determined from Eq. (D1a) for the ultrathin case and from Eq. (D2a) for the low-anisotropy case. For the larger field, the frequencies of the DE band for all the wave vectors are higher than those of the BVMW band. However, as the value of the magnetic field decreases, the frequencies of the DE band for wave vectors around κ^* decrease significantly, and the global minimum of the dispersion relation occurs for the DE configuration; see the red lines in Figs. 11(a) and 11(b). The estimated κ^* values agree well with the analytical values, according to Eqs. (D1c) and (D2d), which confirms the validity of the interpretation that the softening DE mode around κ^* mediates the formation of the stripe domain pattern parallel to applied field direction, which is expected from experiments.

TABLE I. Absolute and normalized parameters used throughout the work. All parameters that appear with an asterisk refer to the critical values at the SRTs. In magnetization dynamics it corresponds to the situation when both Eqs. (2a) and (2b) are satisfied. For all parameters that appear with the "min" subscript throughout the text, only Eq. (2a) is satisfied.

	Absolute	Normalized
Exchange length		$l_{\mathrm{ex}} = \sqrt{\dfrac{2A_{\mathrm{ex}}}{\mu_0 M_{\mathrm{s}}^2}}$
DMI length		$l_{\mathrm{DM}} = \dfrac{2D}{\mu_0 M_{\mathrm{s}}^2}$
Magnetic field	H	$h = \dfrac{H}{M_{\mathrm{s}}}$
Anisotropy (quality factor)	K_u	$Q = \dfrac{2K_{\mathrm{u}}}{\mu_0 M_{\mathrm{s}}^2}$
Film thickness	d	$d_{\mathrm{ex}} = \dfrac{d}{l_{\mathrm{ex}}}$
DMI constant	D	$D_{\mathrm{ex}} = \dfrac{l_{\mathrm{DM}}}{l_{\mathrm{ex}}}$
SW wave number	k	$\kappa = kd$
SW frequency	f	$\dfrac{f}{f_0}, f_0 = \dfrac{\gamma \mu_0 M_{\mathrm{s}}}{2\pi}$
SW wavelength	$\Lambda = \dfrac{2\pi}{k}$	$\Lambda_{\mathrm{ex}} = \dfrac{2\pi d_{\mathrm{ex}}}{\kappa}$
Equilibrium domain period	p	$p_{\mathrm{ex}} = \dfrac{p}{l_{\mathrm{ex}}}$
Critical period	$p^* = \Lambda^*$	$p_{\mathrm{ex}}^* = \Lambda_{\mathrm{ex}}^*$

APPENDIX F: NORMALIZED PARAMETERS AND SCALABILITY OF THE RESULTS

The system of normalized units used throughout this paper and listed in Table I seems to be universal and can be employed for various materials. In the main text, we present many effects (such as the various types of SRT) that occur for specific sets of h, Q, D_{ex}, and d_{ex} values. However, the same set of reduced parameters can be realized for different materials, providing different values of M_{ex}, A_{ex}, and γ. Using the same set of h, Q, D_{ex}, and d_{ex} values, we simulated the dispersion relations for YIG and Co to obtain identical results. In particular, the thickness $d_{\mathrm{ex}} = 11.9$ that corresponds to $d = 200$ nm for YIG can also be realized in a 38.1-nm-thick Co film; $d_{\mathrm{ex}} = 0.624$, corresponding to $d = 2$ nm for Co, can be realized in a 10.5-nm-thick YIG film. On the other hand, $D_{\mathrm{ex}} = 0.246$ corresponds to $D = 1$ mJ/m^2 in Co or 53.3μJ^2 in YIG. Typical material parameters are usually within some limited range of a few orders of magnitude (for example, typical values of l_{ex} are of the order of 10^0–10^1 nm [49]). Nevertheless, as a test, we checked our formalism for absolutely fictitious material, with $M_{\mathrm{s}} = 1$ A/m, $A_{\mathrm{ex}} = 1$ J/m, and $\gamma = 1$ rad/T/s, and providing appropriate scaling of the other quantities, we yielded identical results, both in statics and dynamics.

[1] L. N. Trefethen, A. E. Trefethen, S. C. Reddy, and T. A. Driscoll, Science **261**, 578 (1993).

[2] M. C. Cross and P. C. Hohenberg, Rev. Mod. Phys. **65**, 851 (1993).

[3] L. M. Pismen, Patterns and interfaces in dissipative dynamics, *Encyclopedia of Complexity and Systems Science*, edited by R. Meyers (Springer, New York, 2009), pp. 6459–6476.

[4] M. A. I. Grobas, M. Polin, and M. Asally, eLife **10**, e62632 (2021).

[5] Z. You, A. Baskaran, and M. C. Marchetti, Proc. Natl. Acad. Sci. (USA) **117**, 19767 (2020).

[6] M. Fruchart, R. Hanai, P. B. Littlewood, and V. Vitelli, Nature (London) **592**, 363 (2021).

[7] A. Hubert and R. Schäfer, *Magnetic Domains: The Analysis of Magnetic Microstructures* (Springer, Berlin, Heidelberg, 1998).

[8] E. Y. Vedmedenko, L. Udvardi, P. Weinberger, and R. Wiesendanger, Phys. Rev. B **75**, 104431 (2007).

[9] A. V. Chumak, V. I. Vasyuchka, A. A. Serga, and B. Hillebrands, Nat. Phys. **11**, 453 (2015).

[10] A. Barman, S. Mondal, S. Sahoo, and A. De, J. Appl. Phys. **128**, 170901 (2020).

[11] P. Pirro, V. I. Vasyuchka, A. A. Serga, and B. Hillebrands, Nat. Rev. Mater. **6**, 1114 (2021).

[12] S. Neusser and D. Grundler, Adv. Mater. **21**, 2927 (2009).

[13] S. Saha, R. Mandal, S. Barman, D. Kumar, B. Rana, Y. Fukuma, S. Sugimoto, Y. Otani, and A. Barman, Adv. Funct. Mater. **23**, 2378 (2013).

[14] S. Watanabe, V. S. Bhat, K. Baumgaertl, and D. Grundler, Adv. Funct. Mater. **30**, 2001388 (2020).

[15] C. Banerjee, P. Gruszecki, J. W. Klos, O. Hellwig, M. Krawczyk, and A. Barman, Phys. Rev. B **96**, 024421 (2017).

[16] E. Albisetti, S. Tacchi, R. Silvani, G. Scaramuzzi, S. Finizio, S. Wintz, C. Rinaldi, M. Cantoni, J. Raabe, G. Carlotti *et al.*, Adv. Mater. **32**, 1906439 (2020).

[17] H. Yu, J. Xiao, and H. Schultheiss, Phys. Rep. **905**, 1 (2021).

[18] M. Mruczkiewicz and P. Gruszecki, Solid State Phys. **72**, 1 (2021).

[19] K. Szulc, S. Tacchi, A. Hierro-Rodríguez, J. Díaz, P. Gruszecki, P. Graczyk, C. Quirós, D. Markó, J. I. Martín, M. Vélez *et al.*, ACS Nano **16**, 14168 (2022).

[20] G. Leaf, H. Kaper, M. Yan, V. Novosad, P. Vavassori, R. E. Camley, and M. Grimsditch, Phys. Rev. Lett. **96**, 017201 (2006).

[21] M. Bailleul, D. Olligs, and C. Fermon, Phys. Rev. Lett. **91**, 137204 (2003).

[22] F. Montoncello, L. Giovannini, F. Nizzoli, P. Vavassori, and M. Grimsditch, Phys. Rev. B **77**, 214402 (2008).

[23] C. Ríos-Venegas, F. Brevis, R. A. Gallardo, and P. Landeros, Phys. Rev. B **105**, 224403 (2022).

[24] J. Müller, A. Rosch, and M. Garst, New J. Phys. **18**, 065006 (2016).

[25] M. Grassi, M. Geilen, K. A. Oukaci, Y. Henry, D. Lacour, D. Stoeffler, M. Hehn, P. Pirro, and M. Bailleul, Phys. Rev. B **105**, 094444 (2022).

[26] A. Aharoni, *Introduction to the Theory of Ferromagnetism* (Clarendon, 2001).

[27] J.-H. Moon, S.-M. Seo, K.-J. Lee, K.-W. Kim, J. Ryu, H.-W. Lee, R. D. McMichael, and M. D. Stiles, Phys. Rev. B **88**, 184404 (2013).

[28] H. T. Nembach, J. M. Shaw, M. Weiler, E. Jué, and T. J. Silva, Nat. Phys. **11**, 825 (2015).

[29] K. Di, V. L. Zhang, H. S. Lim, S. C. Ng, M. H. Kuok, J. Yu, J. Yoon, X. Qiu, and H. Yang, Phys. Rev. Lett. **114**, 047201 (2015).

[30] H. S. Körner, J. Stigloher, H. G. Bauer, H. Hata, T. Taniguchi, T. Moriyama, T. Ono, and C. H. Back, Phys. Rev. B **92**, 220413(R) (2015).

[31] S. Tacchi, R. E. Troncoso, M. Ahlberg, G. Gubbiotti, M. Madami, J. Åkerman, and P. Landeros, Phys. Rev. Lett. **118**, 147201 (2017).

[32] M. Kisielewski, A. Maziewski, V. Zablotskii, T. Polyakova, J. M. Garcia, A. Wawro, and L. T. Baczewski, J. Appl. Phys. **93**, 6966 (2003).

[33] M. Kisielewski, A. Maziewski, T. Polyakova, and V. Zablotskii, Phys. Rev. B **69**, 184419 (2004).

[34] J. Kisielewski, M. Kisielewski, V. Zablotskii, A. Dejneka, and A. Maziewski, New J. Phys. **21**, 093022 (2019).

[35] M. Belmeguenai, J.-P. Adam, Y. Roussigné, S. Eimer, T. Devolder, J.-V. Kim, S. M. Cherif, A. Stashkevich, and A. Thiaville, Phys. Rev. B **91**, 180405(R) (2015).

[36] B. A. Kalinikos, M. P. Kostylev, N. V. Kozhus, and A. N. Slavin, J. Phys.: Condens. Matter **2**, 9861 (1990).

[37] A. Vansteenkiste, J. Leliaert, M. Dvornik, M. Helsen, F. Garcia-Sanchez, and B. Van Waeyenberge, AIP Adv. **4**, 107133 (2014).

[38] D. V. Else, C. Monroe, C. Nayak, and N. Y. Yao, Annu. Rev. Condens. Matter Phys. **11**, 467 (2020).

[39] N. Y. Yao, C. Nayak, L. Balents, and M. P. Zaletel, Nat. Phys. **16**, 438 (2020).

[40] N. Träger, P. Gruszecki, F. Lisiecki, F. Groß, J. Förster, M. Weigand, H. Głowiński, P. Kuświk, J. Dubowik, G. Schütz *et al.*, Phys. Rev. Lett. **126**, 057201 (2021).

[41] See Supplemental Material at http://link.aps.org/supplemental/10.1103/PhysRevB.107.134416 for the time evolution of the pattern formation in ultrathin magnetic film after a low-amplitude localized microwave magnetic field pulse of different amplitudes, with or without Dzyaloshinskii-Moriya interaction.

[42] S. Autti, P. J. Heikkinen, J. Nissinen, J. T. Mäkinen, G. E. Volovik, V. V. Zavyalov, and V. B. Eltsov, Nat. Commun. **13**, 3090 (2022).

[43] M. Kisielewski, A. Maziewski, and V. Zablotskii, J. Magn. Magn. Mater. **316**, 277 (2007).

[44] P. Mazalski, B. Anastaziak, P. Kuświk, Z. Kurant, I. Sveklo, and A. Maziewski, J. Magn. Magn. Mater. **508**, 166871 (2020).

[45] A. Hubert, Physica Status Solidi B **32**, 519 (1969).

[46] N. Träger, F. Lisiecki, R. Lawitzki, M. Weigand, H. Głowiński, G. Schütz, G. Schmitz, P. Kuświk, M. Krawczyk, J. Gräfe *et al.*, Phys. Rev. B **103**, 014430 (2021).

[47] S. Ding, A. Ross, R. Lebrun, S. Becker, K. Lee, I. Boventer, S. Das, Y. Kurokawa, S. Gupta, J. Yang *et al.*, Phys. Rev. B **100**, 100406(R) (2019).

[48] J. Rychły, P. Gruszecki, M. Mruczkiewicz, J. W. Kłos, S. Mamica, and M. Krawczyk, Low Temp. Phys. **41**, 745 (2015).

[49] R. Skomski, J. Phys.: Condens. Matter **15**, R841 (2003).